PAPER • OPEN ACCESS

Dynamical instability of 3D stationary and traveling planar dark solitons

View the article online for updates and enhancements.

Dynamical instability of 3D stationary and traveling planar dark solitons

T Mithun[1], **A R Fritsch[2]**, **I B Spielman[2],*** and **P G Kevrekidis[1],***

[1] Department of Mathematics and Statistics, University of Massachusetts, Amherst, MA 01003-4515, United States of America
[2] Joint Quantum Institute, National Institute of Standards and Technology, and University of Maryland, Gaithersburg, MD 20899, United States of America

E-mail: ian.spielman@nist.gov and kevrekid@umass.edu

CrossMark

Abstract

Here we revisit the topic of stationary and propagating solitonic excitations in self-repulsive three-dimensional (3D) Bose–Einstein condensates by quantitatively comparing theoretical analysis and associated numerical computations with our experimental results. Motivated by numerous experimental efforts, including our own herein, we use fully 3D numerical simulations to explore the existence, stability, and evolution dynamics of planar dark solitons. This also allows us to examine their instability-induced decay products including solitonic vortices and vortex rings. In the trapped case and with no adjustable parameters, our numerical findings are in correspondence with experimentally observed coherent structures. Without a longitudinal trap, we identify numerically exact traveling solutions and quantify how their transverse destabilization threshold changes as a function of the solitary wave speed.

Supplementary material for this article is available online

(Some figures may appear in colour only in the online journal)

1. Introduction

Dark solitonic structures emerge ubiquitously in systems that combine dispersion with a self-defocusing nonlinearity. Numerous physical examples encompassing these properties prominently include atomic Bose–Einstein condensates (BECs) [1, 2], and nonlinear Kerr (and generalized non-Kerr) media [3]. More broadly, solitonic structures also arise in mechanical lattices of coupled pendula [4], electrical

transmission lines [5], microwave magnetic thin films [6, 7], acoustic waveguides of Helmholtz resonators [8], surface water waves [9], nematic liquid crystals [10], and BECs with dissipation [11] among others [12, 13]. Outside of these closed systems, solitonic waves are even present in media balancing gain and loss, such as polariton fluids in semiconductor microcavities [14]. The presence of solitary waves in such disparate contexts attests to the breadth of their relevance and the generality of the central mechanisms leading to their creation. In particular, atomic BECs hold a central role amongst these systems owing to their highly tunable interaction Hamiltonians, the control of dimensionality and potential landscapes, as well as the diverse available mechanisms for creating excitations [1, 15, 16].

There are different ways BECs are used to create solitonic states. For example, dragging a laser beam through

* Authors to whom any correspondence should be addressed.

a BEC [17], phase-imprinting [18–20], and matter-wave interference [21, 22]. More recent experiments showed control of both the position and velocity of soliton [23], with contemporary theoretical studies exploring two-dimensional (2D) and three-dimensional (3D) solitary waves in detail [24, 25]. The intriguing dynamics of the resulting structures, including their breakup into vortical patterns [26, 27] (even in superfluid Fermi gases [28]) and their analogues in relativistic systems [29] is a subject of wide investigation and has a wide variety of potential applications ranging from atomic matter-wave interferometers [30] to producing two-level qubit systems [31]. Much of this experimental and theoretical effort is summarized in references [1, 2]. Relevant recent work has also touched upon issues of dark soliton instabilities [32], the inclusion of the effects of localized dissipation [33], or of the dynamics in relativistic BEC settings [34].

In the present work, we revisit dark solitary waves in 3D repulsively interacting BECs highly elongated along the longitudinal axes $\mathbf{e}_z$. These waves are associated with a reduction in the local atomic density accompanied by a modification of the condensate phase. In elongated systems, vortex rings have a similar density distribution but with a ring-shaped phase singularity [1, 35]. The simplest example is a planar (or kink) soliton where the density is reduced to be two dimensional on a plane normal to the soliton's direction of propagation. By contrast, a solitonic vortex is a highly anisotropic vortex with a linear phase-singularity [1]. The potential conversion of kink solitons into these excitations is of wide interest [36–41].

We begin by comparing experimentally observed solitary waves with 3D numerical simulations [42] computed with no adjustable parameters. Motivated by this comparison, we theoretically explore the related 3D case of a longitudinally traveling solitonic wave. This approach is limited to the case of a system that is transversely confined but longitudinally infinite. Then, we compute the relevant Bogolyubov-de Gennes (BdG) modes to identify the onset of transverse instability and to quantify the growth rate of the unstable mode. This process confirms the prediction of reference [43] that the interval of stability of kink solitons increases as their speed approaches the local speed of sound c. Finally in the unstable regime, we numerically follow the exponential growth of the unstable mode to its ultimate conversion to vortex structures.

2. Experimental motivation: phase engineering and in-trap motion

In the present work, we model the experimental procedure in [23] which describes a new wavefunction engineering approach for launching solitons in atomic BECs and show that dark planar solitons are first created and then relax into solitonic vortices.

The experiments started with $N = 2.4 \times 10^5$ ^{87}Rb BECs confined in an optical dipole trap with frequencies $(\omega_x, \omega_y, \omega_z) = 2\pi \times (94.73, 153.23, 9.1)$ Hz and chemical potential $\mu = h \times 1.1$ kHz. We created solitonic excitations by combining conventional phase imprinting with density engineering,

i.e. wavefunction engineering, yielding solitonic excitations with a wide range of initial velocities [23].

We consider the fully 3D Gross-Pitaveskii model (GPE), describing these experiments [15, 16]

$$i\hbar \frac{\partial \psi}{\partial t} = \left[-\frac{\hbar^2}{2m}\nabla^2 + V(\mathbf{r}) + g|\psi|^2 \right]\psi. \tag{1}$$

Here, ψ is normalized to the total atom number N_{3D}, interaction constant and potential are defined as $g = 4\pi\hbar^2 a_s/m$ and $V(\mathbf{r}) = m(\omega_x^2 x^2 + \omega_y^2 y^2 + \omega_z^2 z^2)/2 + V_{step}(t)\mathcal{H}(z)$, respectively, where $\mathcal{H}(z)$ represents the Heaviside function. We fix the magnitude of the step potential $V_{step}(t)$ to be 0 except during the phase-imprinting pulse when it is $h \times 5.5$ kHz.

We simulate the experiments using the parameters described above and create solitons via the phase imprinting method: applying a potential generated with an infinitely sharp edge (smaller than the BEC healing length) to half of the BEC. We note that the density engineering method is implemented in the experiment to circumvent technical limitations, given that the BEC healing length is typically much smaller than the optical resolution of the imaging systems used for phase imprinting, which is not the case in numerical simulations. We found that the idealization of a step potential centered at $z = 0$ and amplitude V_{step}, is sufficient to reproduce the experimental results. This indirectly demonstrates the efficacy of the experimental approach.

Figure 1 shows the 3D density projected onto the $\mathbf{e}_x - \mathbf{e}_z$ and $\mathbf{e}_y - \mathbf{e}_z$ planes, i.e. $|\psi(x,z)|^2$ and $|\psi(y,z)|^2$, and the associated planar phase cuts, immediately following the application of V_{step} for a phase imprinting time $t_p = 140$ μs. The phase-imprinted planar dark soliton subsequently evolves into a vortex ring as shown in [44]. This ring eventually decays [45] into a pair of solitonic vortices aligned along the direction of stronger transverse confinement and exhibits a large amplitude oscillation [44]. The weak interaction of the resulting structures with the background of excited phonons leads to effective (apparent) dissipative longitudinal dynamics and to the selection of two separate trajectories, one for each solitonic vortex as shown in figures 2 and 3. In the experimental results, over long times, the amplitude of oscillation appears to be growing, possibly reflecting the (weak) anti-damping effect due to the thermal fraction [46]. Both the numerical and experimental results (black crosses) find an oscillation frequency ω_s far from the 'canonical' result of $\omega_s = \omega_z/\sqrt{2}$ for planar solitons [2, 47]. Instead, the solitonic vortex oscillation frequency is significantly reduced [23, 24], e.g. by a factor of about 3 in comparison to ω_z, as shown in the bottom panel of figure 3. More generally, in line with [24], we find that the relevant reduction is a function of the chemical potential, and the general agreement between the experimental data and the numerical simulations supports solitonic vortex pair formation from the method of phase imprinting. This experiment-theory correspondence prompts us to further explore the stability of planar solitons and their transformation into other structures.
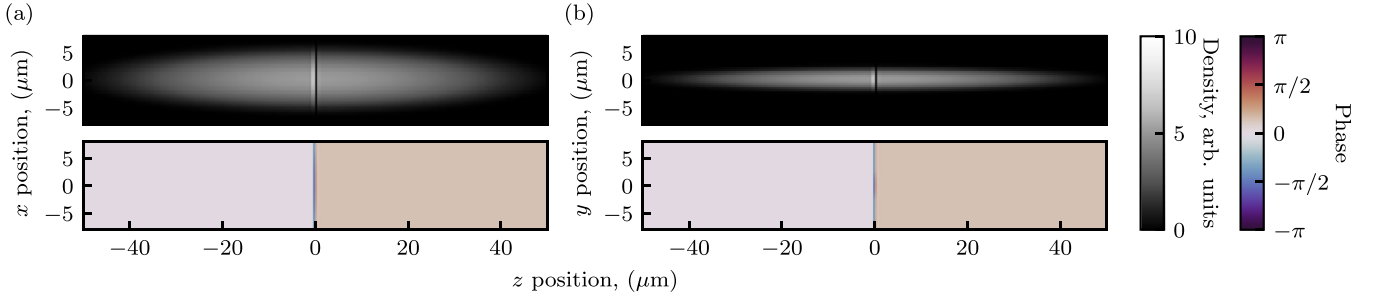
Figure 1. Integrated GPE wavefunction density (top) and phase cross-section (bottom) evaluated immediately after a $t_p = 140\,\mu$s phase imprint. (a) and (b) plot $|\psi(x,z)|^2$ and $|\psi(y,z)|^2$ respectively.
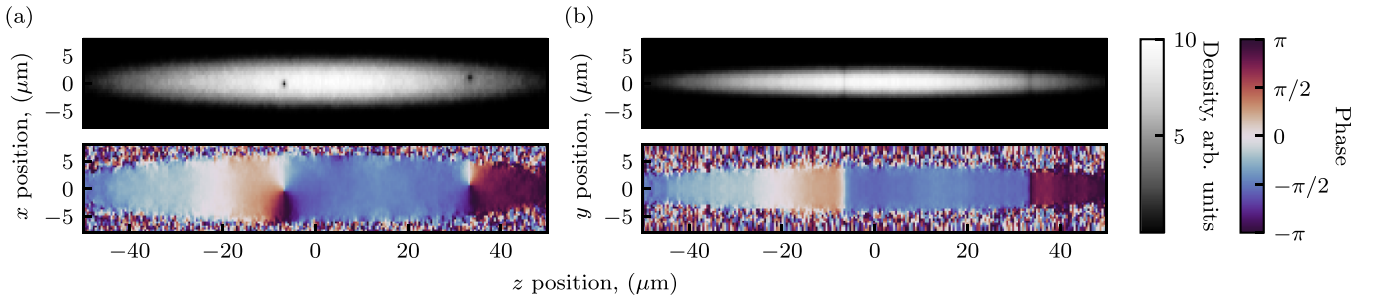

Figure 2. Integrated GPE wavefunction density (top) along with phase (bottom) cross-sections evaluated 400 ms after a $t_p = 140\,\mu$s phase imprint. (a) Plots the $|\psi|^2$ projection and associated cross-sections in the $\mathbf{e}_x - \mathbf{e}_z$ plane and (b) plots $\mathbf{e}_y - \mathbf{e}_z$ quantities.
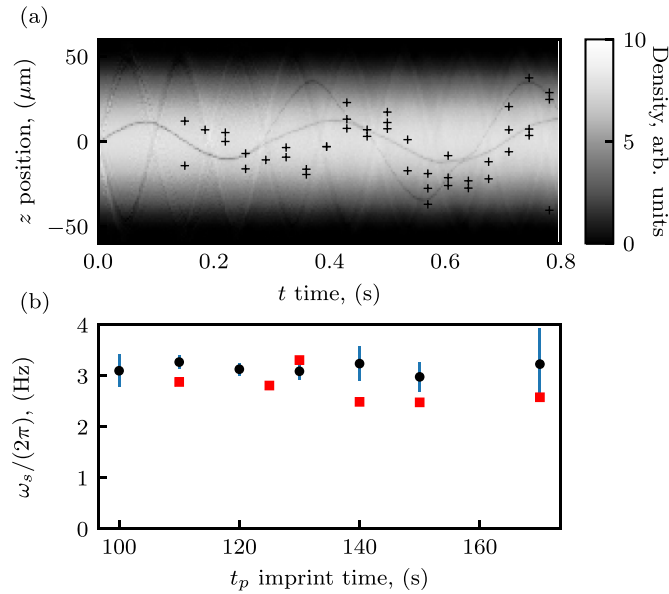

Figure 3. Oscillation of the solitonic vortices (a) and oscillation frequencies (b). The black symbols on the grey scale integrated GPE wavefunction density in $\mathbf{e}_z - t$ plane of (a) represent experimental data. Every set of experimental parameters was repeated three times, and a symbol is present for each clearly identified solitonic excitation. In cases in which more than one solitonic excitation was found in a single image we chose the position of the deepest depletion. The simulations use $t_p = 140\,\mu$s. The symbols, red squares and black circles, in (b) represent GPE and experimental calculations, respectively, where the error bar represents the single-σ uncertainty obtained from the sinusoidal fits.

3. Stability of planar dark solitons

In this section we study the stability of dark solitary waves using a dimensionless version of equation (1)

$$i\frac{\partial \psi'}{\partial t'} = \left[-\frac{1}{2}(\nabla')^2 + V'(\mathbf{r}') + g'|\psi'|^2\right]\psi', \qquad (2)$$

in terms of the dimensionless quantities $t' = \omega_\perp t$, $\mathbf{r}' = \mathbf{r}/a_\perp$, $\psi' = a_\perp^{3/2}\psi$, $V(\mathbf{r}') = [l_x^2(x')^2 + l_y^2(y')^2 + l_z^2(z')^2]/2$, $g' = 4\pi a_s/a_\perp$, and $\mu' = \mu/(\hbar\omega_\perp)$. Here, we use the transverse degrees of freedom to define the natural units of frequency $\omega_\perp = \sqrt{\omega_x \omega_y}$ and length $a_\perp = \sqrt{\hbar/(m\omega_\perp)}$. In addition, we introduce anisotropy parameters $l_x = \omega_x/\omega_\perp$, $l_y = \omega_y/\omega_\perp$ and $l_z = \omega_z/\omega_\perp$.
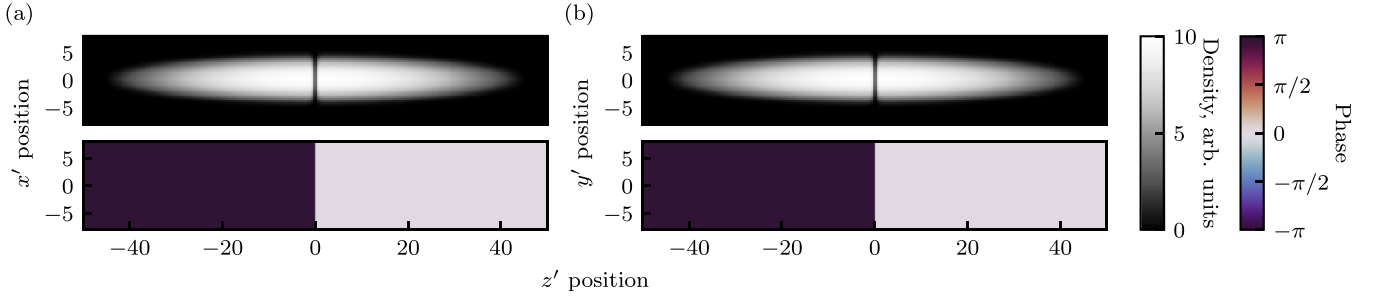
Figure 4. Condensate GPE density of the equation (5) (top) and phase cross-section (bottom) show the stationary 3D dark soliton solution for $\omega_\perp/(2\pi) = 100$ Hz, where $\omega_x = \omega_y$ and $v = 0$. The lower panel shows the soliton phase jump from π (dark) to 0 (light). (a) and (b) plot $|\psi'(x', 0, z')|^2$ and $|\psi'(0, y', z')|^2$ respectively.

In line with the last section, we use a chemical potential $\mu = h \times 1.1$ kHz, longitudinal frequency $\omega_z/(2\pi) = 10$ Hz, and transverse frequency ranging from $\omega_\perp/(2\pi) = 100$ Hz to 1 kHz. In what follows, we take $\omega_x = \omega_y$ for simplicity.

The 1D counterpart of equation (1) with $V = 0$ supports the dark soliton solution [1]

$$\psi_k'(z', t') = \sqrt{n_0} \left[B \tanh(\zeta) + iA \right] e^{i(kz' - \omega t')}. \quad (3)$$

Here, $n_0 = \mu'$, $\zeta = \sqrt{n_0} B[z' - z_0(t')]$, $z_0 = vt' + Z_0$, $v = A\sqrt{n_0} + k$, $\omega = k^2/2 + n_0$ and $A^2 + B^2 = 1$, and restrict ourselves to $k = 0$ solutions (of a stationary background). The remaining properties have the standard meaning, i.e. v is the soliton speed, n_0 the background density, z_0 marks the center of mass (and Z_0 is its initial value), while B is associated with the inverse solitonic width [1].

3.1. Stationary solutions

In the presence of a trap, the wavefunction for a 3D stationary solution is approximately

$$\psi'(\mathbf{r}', t') = \psi_{ds}(z') \Phi(\mathbf{r}') e^{-i\mu' t'}, \quad (4)$$

where $\Phi(\mathbf{r}')$ represents the ground state Thomas-Fermi (TF) wavefunction [15, 16] and ψ_{ds} represents the stationary dark soliton from equation (3), associated with $A = v = 0$. Using equation (4) as an initial guess for a root finding algorithm, we obtain numerically exact solutions by solving

$$\mathcal{F}(\psi') = \left[-\frac{1}{2} \nabla^2 + V(\mathbf{r}') + g'|\psi'|^2 - \mu' \right] \psi' = 0. \quad (5)$$

Figure 4 shows the solution of equation (5) for $\omega_\perp/(2\pi) = 100$ Hz. We now explore both the stable and unstable modes of ψ' by identifying the eigenvalues associated with the BdG equations [1, 15, 16] for the parameter range of $\omega_\perp$. For relevant details, see the appendix A. An eigenvalue λ has a real part denoted by λ_r and an imaginary part denoted by λ_i. It is important to recall that a non-vanishing λ_r, given the Hamiltonian nature of our GPE (2), is tantamount to the presence of a dynamical instability.

There exist two limiting cases for the stability problem of the dark solitary waves in a trapped condensate, more specifically, the TF limit at large chemical potential μ' and the linear limit at small μ'. As is well-known [1] in the 1D limit of the GPE model, the anomalous mode (ω_0), corresponding to negative energy is associated with the oscillation of the single dark soliton with a frequency of $\approx l_z/\sqrt{2}$ [47]. The other modes ω_n (associated with the vibration modes of the background cloud) are expected to approach the frequencies of $l_z\sqrt{n(n+1)/2}$ [16]. On the other hand, in the linear limit of vanishing density $|\psi'|^2 \to 0$, the eigenvalue problem of equation (1) reduces to that of a *linear* quantum harmonic oscillator with corresponding energies of eigenmodes $|k, l, m\rangle$

$$E_{k,l,m} = \left(k + \frac{1}{2} \right) l_x + \left(l + \frac{1}{2} \right) l_y + \left(m + \frac{1}{2} \right) l_z. \quad (6)$$

A single dark soliton at $z' = 0$ (pertaining to the $|0, 0, 1\rangle$ in the linear limit) has energy $E_{0,0,1} = (l_x + l_y + 3\,l_z)/2$. To explore the validity of these predictions, we rescale the imaginary eigenvalues by l_z and show the corresponding results in figure 5. Indeed, our numerically calculated imaginary eigenvalues confirm the expectations on the basis of the 1D predictions, as our numerical continuation results approach progressively the 1D TF limit as $\omega_\perp$ increases. We note that the chemical potential controls the approach to the TF limit for the present setting. The mode responsible for the instability of the planar dark soliton appears as a nearly vertical dashed black line in figure 5.

The analysis of real eigenvalues displayed in figure 6 shows that, as $\omega_\perp$ decreases (going away from the above mentioned quasi-1D limit), there exists an instability window for smaller values of the relevant parameter. The critical $\omega_\perp$, namely $\omega_\perp^c$, at which λ_r crosses zero is at $2\pi \times 418$ Hz. Figure 7 shows the eigenvector corresponding to the largest real eigenvalue of equation (A3) for the parameter $\omega_\perp/(2\pi) = 415$ Hz and $\omega_x = \omega_y$. Indeed, on the basis of the relevant unstable eigenmode, we expect the planar dark solitary wave structure to break its axial symmetry and reshape itself in the form of a vortex ring as a result of the relevant growing mode, recalling that the latter only breaks up toward a pair of solitonic vortices considerably later in the dynamical evolution. It is interesting to highlight that the above instability manifestation appears to be a natural 3D generalization of the destabilization of a 2D
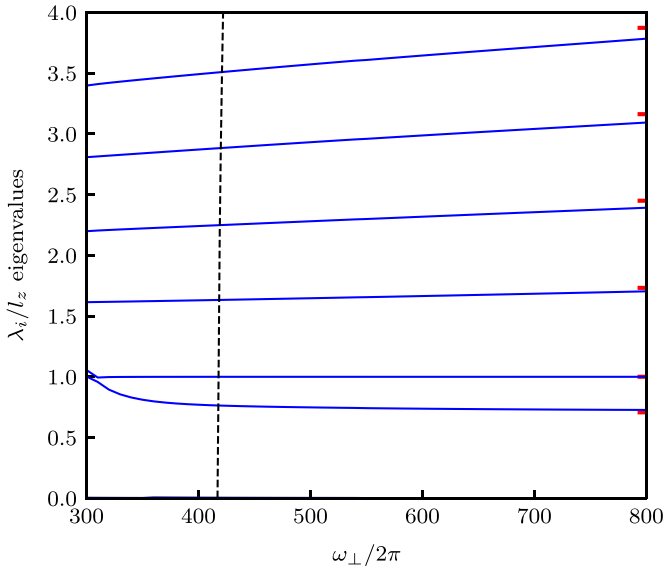
Figure 5. Imaginary eigenvalues λ_i obtained from the BdG analysis plotted as a function of $\omega_\perp$ for $\omega_x = \omega_y$. The vertical dashed black line represents the mode responsible for instability of the planar dark soliton, while blue lines represent stable modes. In the limit of large $\omega_\perp$, the 1D analytically available results, indicated by the red short lines, are retrieved (see text for further details).
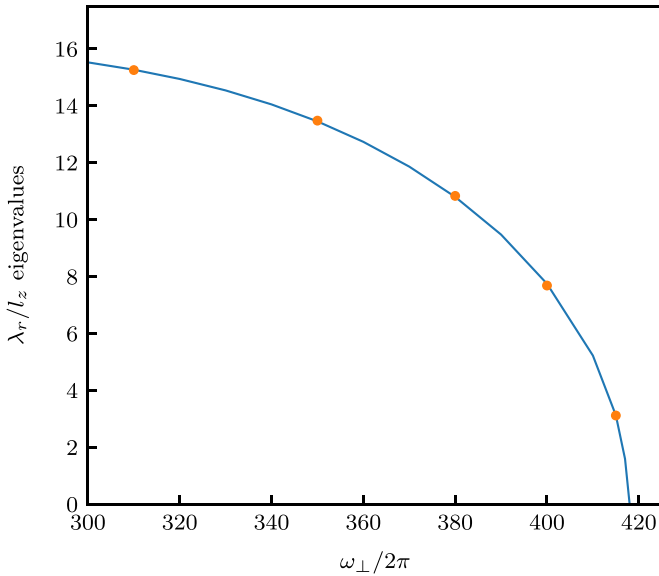

Figure 6. The largest real eigenvalue λ_r, associated with the instability of the stationary, planar dark soliton, as a function of $\omega_\perp$ for $\omega_x = \omega_y$. The red circles are obtained from GPE dynamics and the blue line represents BdG analysis.

planar dark soliton toward the formation of a vortex dipole, explored from a bifurcation theory perspective, e.g. in [48, 49].

The most unstable eigenvalue (the one bearing the largest real part) can be computed from the GPE dynamics starting from the perturbed steady state solutions of equation (5) [50]. We evolve such waveforms starting with a small perturbation $\delta\psi$ [$\approx 10^{-10}$ relative to the max($|\psi'|$)]. As expected

from the linear stability analysis, we find that this perturbation grows exponentially as $\psi' = \psi'_0 \exp(\lambda_r t')$ with an instability growth time $\tau = -\log(|\delta\psi|)/\lambda_r$. The computed growth rate λ_r via this 'direct integration' approach, indicated by circles on figure 6, matches well with the largest eigenvalues obtained from the spectral analysis of the BdG equations, thus confirming the robustness of our numerical findings. The GPE dynamics for different $\omega_\perp$ shows that the strength of transverse confinement determines the resulting wave structures induced by the transverse instability of dark solitary waves. We generally find that tighter confinement favors the formation of a solitonic vortex, while looser traps result in a long-lived vortex ring. Figures 8 and 9 show the vortex ring and solitonic vortex generated during the GPE dynamics with $\omega_\perp/(2\pi) = 100$ Hz and $\omega_\perp/(2\pi) = 250$ Hz. Their existence can be further confirmed from the 3D condensate densities shown in figure 10. The single solitonic vortex formation from the imprinted dark soliton for higher $\omega_\perp$ is due to the asymmetric flow (see figure 7) arising from the transverse instability that leads to the bending of density on the $\mathbf{e}_y - \mathbf{e}_z$ plane [41].

3.2. Traveling solutions

We now consider the case of traveling solitary waves. In this case, we find the steady solution of the 3D-GPE equation in the so-called co-traveling frame variant of equation (5) for which

$$\mathcal{F}(\psi') = \left[-\frac{1}{2}\nabla^2 + iv\frac{\partial}{\partial z'} + V(\mathbf{r}') + g'|\psi'|^2 - \mu' \right]\psi' = 0$$

and v represents the soliton velocity i.e. by seeking a numerically exact stationary solution in the co-traveling frame along $\mathbf{e}_z$, we obtain a traveling solution of the original frame. In this case, we fix the longitudinal length $L_z = 120a_\perp$ and remove the trap along the z-direction, so that genuine traveling can be feasible along this direction. Figure 11 shows the steady state solution for $v = 0.1c_s$, where $c_s = \sqrt{\mu'}$ is the sound velocity, and $\omega_\perp/(2\pi) = 400$ Hz. This shows a phase jump which corresponds to the gray soliton [2] at the $\mathbf{r}' = 0$ plane. The additional phase jump at the boundary is due to the implemented periodic boundary condition.

Importantly, the computation of the traveling planar dark solitary wave solution is accompanied by the solution of the BdG equations to identify the spectral stability of the relevant state. The largest real eigenvalues leading to the unstable dynamics of moving solitons are shown in figure 12 as a function of $\omega_\perp$. As the velocity increases, the λ_r/l_z decreases and, in this way, leads to the increase in the critical transverse frequency ω_c, which is representing the transition point of stable to unstable dynamics. The corresponding chemical potential $\mu_c = \mu/(\hbar\omega_\perp^c)$ is shown in the inset of figure 12 as a function of v/c_s. This corroborates, through detailed 3D computations, the earlier dynamical results of [43]. On the other hand, we find from the GPE dynamics that the transverse instability leads to the formation of solitonic vortices as in the case of
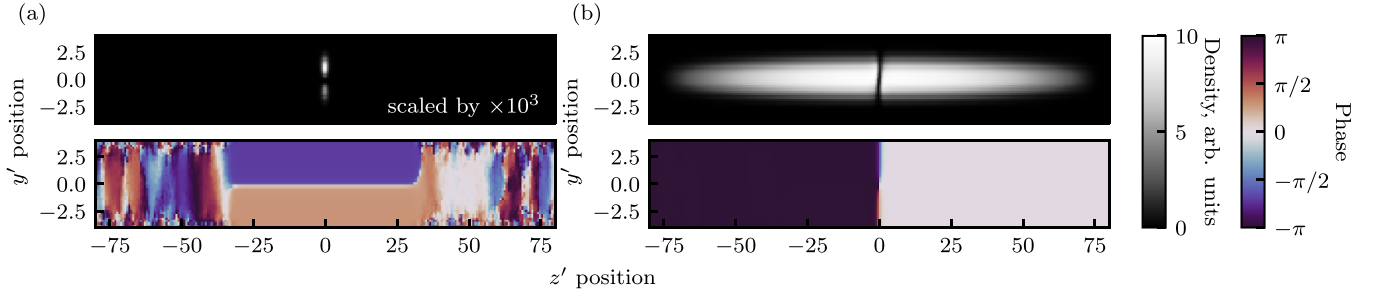
Figure 7. (a) The eigenvector $|\varphi|^2$ corresponds to the largest real eigenvalue of equation (A3) and its phase profile for the parameter $\omega_\perp/(2\pi) = 415$ Hz and $\omega_x = \omega_y$. (b) The density $|\psi' + \epsilon\varphi|^2$, where ψ' is the steady state wavefunction and $\varepsilon = 20$. Lower panels in (a) and (b) show the phase cross-section.
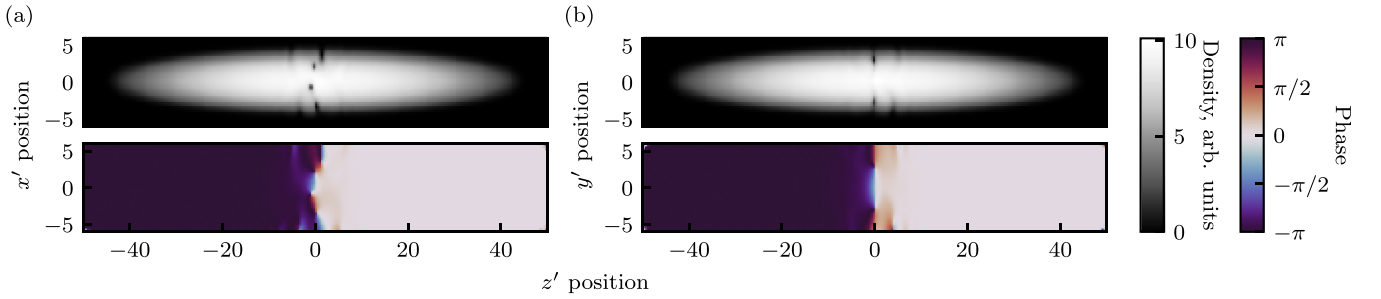

Figure 8. Condensate densities (top) and phase cross-section (bottom) show the existence of a vortex ring at $t' = 15$ after evolving the steady state dark soliton solution. Here, $\omega_\perp/(2\pi) = 100$ Hz and $\omega_x = \omega_y$. (a) and (b) plot $|\psi(x',0,z')|^2$ and $|\psi(0,y',z')|^2$ respectively.
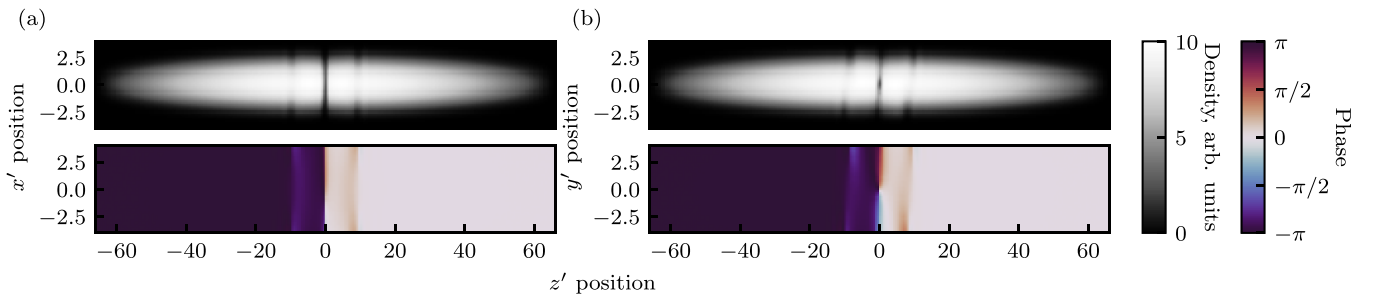

Figure 9. Condensate densities (top) and phase cross-section (bottom) show a solitonic vortex at $t' = 50$ after evolving the steady state dark soliton solution. Here, $\omega_\perp/(2\pi) = 250$ Hz and $\omega_x = \omega_y$. (a) and (b) plot $|\psi'(x',0,z')|^2$ and $|\psi'(0,y',z')|^2$ respectively.
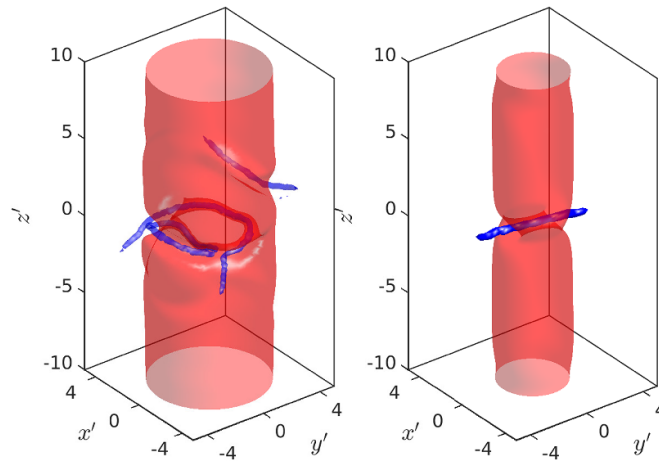

Figure 10. The three dimensional view of the snapshots shown in figures 8 (left) and 9 (right). The red and blue colors represent cuts of constant density and vorticity.
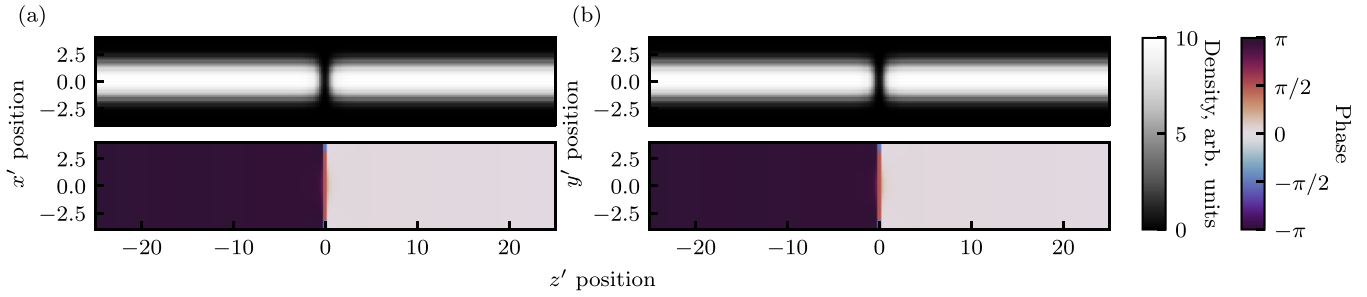
Figure 11. Condensate densities (top) and phase cross-section (bottom) of numerically exact traveling planar dark soliton solution for $\omega_\perp/(2\pi) = 400$ Hz, where $\omega_x = \omega_y$ and $v = 0.1c_s$. (a) and (b) plot $|\psi(x',0,z')|^2$ and $|\psi(0,y',z')|^2$ respectively.
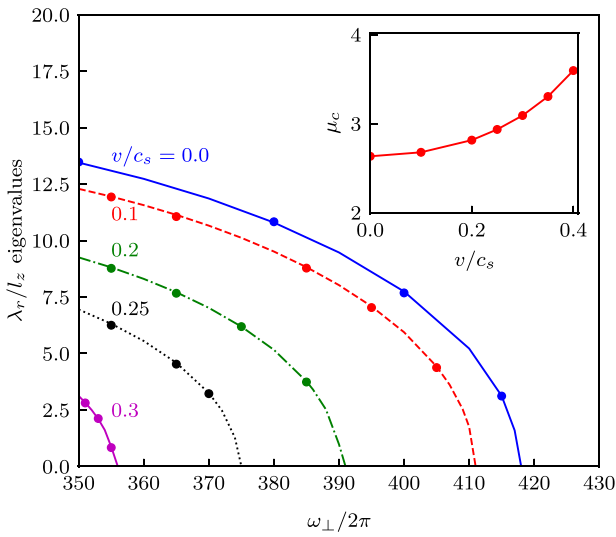

Figure 12. The largest real eigenvalues leading to the unstable dynamics of moving solitons as a function of $\omega_\perp$. The lines of the main figure (top to bottom) represent the cases, $v = (0, 0.1, 0.2, 0.25, 0.3) \times c_s$ obtained from the eigenvalue problem, while circles represent the growth rate obtained from the GPE dynamics. The inset shows the critical chemical potential μ_c as a function of v/c_s.
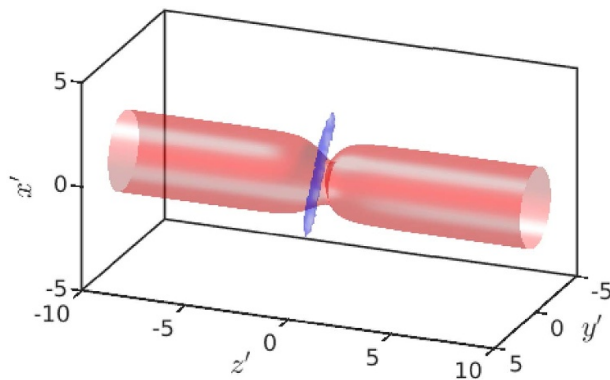

Figure 13. The three dimensional view of condensate density $|\psi'|^2$ at $t' = 80$ for $v = 0.2c_s$. The red and blue colors represent cuts of constant density and vorticity.

$v = 0$. Figure 13 shows the solitonic vortex at $t' = 80$ formed during the dynamical evolution of the condensate density for $v = 0.2c_s$.

4. Conclusions and outlook

In summary, motivated by experimental observations in 3D BECs indicative of the dynamical instability of planar dark solitons, we analyzed the stability of both stationary and traveling planar dark solitons. We first illustrated the comparison of our 3D time-dependent numerical computations with the experimentally observed time-evolution. This indicated that, for the experimental parameters, the phase imprinting of a planar dark soliton gave rise to a vortex ring that subsequently decayed into a solitonic vortex. This finding motivated us to explore the stability of planar dark solitons as a function of the transverse confinement, thereby quantifying the transition from the 3D to the 1D regime. Indeed, for sufficiently strong transverse confinement, our BdG analysis identified the quasi-1D limiting values of the corresponding excitation frequencies. This analysis further captured the destabilization of planar dark solitons in the 3D regime. We identified the most rapidly growing unstable mode in two distinct ways; one by the GPE direct simulation and another by the BdG analysis, and monitored the resulting dynamics leading to the formation of solitonic vortices or vortex rings (depending on the transverse confinement).

Although this problem has been studied from a range of perspectives, there are still numerous open questions. Our primary focus here is on the implications of the transverse confinement. However, these structures are not exact solutions for non-zero longitudinal confinement, therefore their stability and properties as a function of longitudinal confinement merits further study. Moreover, a careful inspection of the movie in [44] raises intriguing questions on the scattering interactions between and overall dynamics of solitonic vortices in confined geometries. In the same vein, the behavior of solitonic structures in box potentials [51], as well as more general (i.e. beyond parabolic) potentials is of considerable current interest. In this case, one can study how structures that are near-exact solutions in the bulk abruptly impinge on the system's edge. Further possibilities could involve localized barriers [52] or even random potentials [53] where the soliton's fate and trajectory are unknown.

Data availability statement

The data that support the findings of this study are available upon reasonable request from the authors.

Acknowledgments

Appendix A. Linearized GP equation

The adimensionalized GPE can be written as

$$i\frac{\partial \psi'}{\partial t'} = \left[-\frac{1}{2}\nabla^2 + V(\mathbf{r}') - \mu' + g'n \right]\psi, \qquad (A1)$$

with $n = |\psi'|^2$. The linearized evolution $\psi' = \psi'_0 + \varepsilon\,\delta\psi$ about the steady state ψ'_0 is described by

$$i\frac{\partial \delta\psi}{\partial t'} = K_R\,\delta\psi + K_I\,\delta\psi^*, \qquad (A2)$$

with

$$K_R = -\frac{1}{2}\nabla^2 + V(\mathbf{r}') - \mu' + 2\,g|\psi'|^2 \quad \text{and} \quad K_I = g'\psi'^2.$$

Finally, for the perturbation $\delta\psi = Pe^{\lambda t'} + Q^* e^{\lambda^* t'}$, the linearized problem

$$i\lambda \begin{pmatrix} P \\ Q \end{pmatrix} = \begin{pmatrix} K_R & K_I \\ -K_I^* & -K_R^* \end{pmatrix} \begin{pmatrix} P \\ Q \end{pmatrix} \qquad (A3)$$

takes on the familiar BdG structure.

ORCID iDs

T Mithun ⦿ https://orcid.org/0000-0003-4341-6439
I B Spielman ⦿ https://orcid.org/0000-0003-1421-8652
P G Kevrekidis ⦿ https://orcid.org/0000-0002-7714-3689

References

[1] Kevrekidis P G, Frantzeskakis D J and Carretero-González R 2015 *The Defocusing Nonlinear Schrödinger Equation: From Dark Solitons to Vortices and Vortex Rings* (Philadelphia, PA: SIAM)

[2] Frantzeskakis D J 2010 Dark solitons in atomic Bose-Einstein condensates: from theory to experiments *J. Phys. A: Math. Theor.* **43** 213001

[3] Kivshar Y S and Luther-Davies B 1998 Dark optical solitons: physics and applications *Phys. Rep.* **298** 81–197

[4] Denardo B, Galvin B, Greenfield A, Larraza A, Putterman S and Wright W 1992 Observations of localized structures in nonlinear lattices: domain walls and kinks *Phys. Rev. Lett.* **68** 1730–3

[5] Marquie P, Bilbault J M and Remoissenet M 1994 Generation of envelope and hole solitons in an experimental transmission line *Phys. Rev.* E **49** 828–35

[6] Chen M, Tsankov M A, Nash J M and Patton C E 1993 Microwave magnetic-envelope dark solitons in yttrium iron garnet thin films *Phys. Rev. Lett.* **70** 1707–10

[7] Kalinikos B A, Scott M M and Patton C E 2000 Self-generation of fundamental dark solitons in magnetic films *Phys. Rev. Lett.* **84** 4697–700

[8] Achilleos V, Richoux O, Theocharis G and Frantzeskakis D J 2015 Acoustic solitons in waveguides with helmholtz resonators: transmission line approach *Phys. Rev.* E **91** 023204

[9] Chabchoub A, Kimmoun O, Branger H, Hoffmann N, Proment D, Onorato M and Akhmediev N 2013 Experimental observation of dark solitons on the surface of water *Phys. Rev. Lett.* **110** 124101

[10] Piccardi A, Alberucci A, Tabiryan N and Assanto G 2011 Dark nematicons *Opt. Lett.* **36** 1356–8

[11] Baals C, Moreno A G, Jiang J, Benary J and Ott H 2021 Stability analysis and attractor dynamics of three-dimensional dark solitons with localized dissipation *Phys. Rev.* A **103** 043304

[12] Ren J, Ilhan O A, Bulut H and Manafian J 2021 Multiple rogue wave, dark, bright and solitary wave solutions to the kpâbbm equation *J. Geom. Phys.* **164** 104159

[13] Feng B, Manafian J, Ilhan O A, Rao A M and Agadi A H 2021 Cross-kink wave, solitary, dark and periodic wave solutions by bilinear and he's variational direct methods for the kpâbbm equation *Int. J. Mod. Phys.* B **35** 2150275

[14] Carusotto I and Ciuti C 2013 Quantum fluids of light *Rev. Mod. Phys.* **85** 299–366

[15] Pethick C J and Smith H 2008 *Bose-Einstein Condensation in Dilute Gases* (Cambridge: Cambridge University Press)

[16] Pitaevskii L and Stringari S 2018 *Bose-Einstein Condensation and Superfluidity* (Oxford: Oxford University Press)

[17] Engels P and Atherton C 2007 Stationary and nonstationary fluid flow of a Bose-Einstein condensate through a penetrable barrier *Phys. Rev. Lett.* **99** 160405

[18] Burger S, Bongs K, Dettmer S, Ertmer W, Sengstock K, Sanpera A, Shlyapnikov G V and Lewenstein M 1999 Dark solitons in Bose-Einstein condensates *Phys. Rev. Lett.* **83** 5198–201

[19] Denschlag J *et al* 2000 Generating solitons by phase engineering of a Bose-Einstein condensate *Science* **287** 97–101

[20] Becker C, Stellmer S, Soltan-Panahi P, Dörscher S, Baumert M, Richter E M, Kronjäger J, Bongs K and Sengstock K 2008 Oscillations and interactions of dark and dark-bright solitons in Bose-Einstein condensates *Nat. Phys.* **4** 496

[21] Weller A, Ronzheimer J P, Gross C, Esteve J, Oberthaler M K, Frantzeskakis D J, Theocharis G and Kevrekidis P G 2008 Experimental observation of oscillating and interacting matter wave dark solitons *Phys. Rev. Lett.* **101** 130401

[22] Theocharis G, Weller A, Ronzheimer J P, Gross C, Oberthaler M K, Kevrekidis P G and Frantzeskakis D J 2010 Multiple atomic dark solitons in cigarshaped Bose-Einstein condensates *Phys. Rev.* A **81** 063604

[23] Fritsch A R, Lu M, Reid G H, Piñeiro A M and Spielman I B 2020 Creating solitons with controllable and near-zero velocity in Bose-Einstein condensates *Phys. Rev.* A **101** 053629

[24] Mateo A M and Brand J 2015 Stability and dispersion relations of three-dimensional solitary waves in trapped Bose-Einstein condensates *New J. Phys.* **17** 125013

[25] Verma G, Rapol U D and Nath R 2017 Generation of dark solitons and their instability dynamics in two-dimensional condensates *Phys. Rev.* A **95** 043618

[26] Anderson B P, Haljan P C, Regal C A, Feder D L, Collins L A, Clark C W and Cornell E A 2001 Watching dark solitons decay into vortex rings in a Bose-Einstein condensate *Phys. Rev. Lett.* **86** 2926–9

[27] Shomroni I, Lahoud E, Levy S and Steinhauer J 2009 Evidence for an oscillating soliton/vortex ring by density engineering of a Bose-Einstein condensate *Nat. Phys.* **5** 193–7

[28] Ku M J H, Ji W, Mukherjee B, Guardado-Sanchez E, Cheuk L W, Yefsah T and Zwierlein M W 2014 Motion of a solitonic vortex in the BEC-BCS crossover *Phys. Rev. Lett.* **113** 065301

[29] Di Mauro Villari L, Galbraith I and Biancalana F 2020 Long-lived nonlinear oscillatory states in interacting relativistic Bose-Einstein condensates *Phys. Rev.* A **102** 033321

[30] Negretti A and Henkel C 2004 Enhanced phase sensitivity and soliton formation in an integrated BEC interferometer *J. Phys. B: At. Mol. Opt. Phys.* **37** L385–90

[31] Shaukat M I, Castro E V, Terças H and Terças H 2017 Quantum dark solitons as qubits in Bose-Einstein condensates *Phys. Rev.* A **95** 053618

[32] Verma G, Rapol U D and Nath R 2017 Generation of dark solitons and their instability dynamics in two-dimensional condensate *Phys. Rev.* A **95** 043618

[33] Baals C, Moreno A G, Jiang J, Benary J and Ott H 2021 Stability analysis and attractor dynamics of three-dimensional dark solitons with localized dissipation *Phys. Rev.* A **103** 043304

[34] Di Mauro Villari L, Galbraith I and Biancalana F 2020 Long-lived nonlinear oscillatory states in interacting relativistic Bose-Einstein condensates *Phys. Rev.* A **102** 033321

[35] Komineas S 2007 Vortex rings and solitary waves in trapped Bose-Einstein condensates *Eur. Phys. J. Spec. Top.* **147** 133–52

[36] Komineas S and Papanicolaou N 2003 Solitons, solitonic vortices and vortex rings in a confined Bose-Einstein condensate *Phys. Rev.* A **68** 043617

[37] Brand J and Reinhardt W P 2002 Solitonic vortices and the fundamental modes of the "snake instability": possibility of observation in the gaseous Bose-Einstein condensate *Phys. Rev.* A **65** 043612

[38] Becker C, Sengstock K, Schmelcher P, Kevrekidis P G and Carretero-González R 2013 Inelastic collisions of solitary waves in anisotropic Bose-Einstein condensates: sling-shot events and expanding collision bubbles *New J. Phys.* **15** 113028

[39] Tylutki M, Donadello S, Serafini S, Pitaevskii L P, Dalfovo F, Lamporesi G and Ferrari G 2015 Solitonic vortices in Bose-Einstein condensates *Eur. Phys. J. Spec. Top.* **224** 577–83

[40] Tsatsos M C, Edmonds M J and Parker N G 2016 Transition from vortices to solitonic vortices in trapped atomic Bose-Einstein condensates *Phys. Rev.* A **94** 023627

[41] Donadello S, Serafini S, Tylutki M, Pitaevskii L P, Dalfovo F, Lamporesi G and Ferrari G 2014 Observation of solitonic vortices in Bose-Einstein condensates *Phys. Rev. Lett.* **113** 065302

[42] Bao W, Jaksch D and Markowich P A 2003 Numerical solution of the Gross-Pitaevskii equation for Bose-Einstein condensation *J. Comput. Phys.* **187** 318–42

[43] Muryshev A, Shlyapnikov G V, Ertmer W, Sengstock K and Lewenstein M 2002 Dynamics of dark solitons in elongated Bose-Einstein condensates *Phys. Rev. Lett.* **89** 110401

[44] See Supplemental Material for corresponding GPE dynamics (https://doi.org/10.1088/1361-648X/ac9e36)

[45] Ticknor C, Wang W and Kevrekidis P G 2018 Spectral and dynamical analysis of a single vortex ring in anisotropic harmonically trapped three-dimensional Bose-Einstein condensates *Phys. Rev.* A **98** 033609

[46] Cockburn S P, Nistazakis H E, Horikis T P, Kevrekidis P G, Proukakis N P and Frantzeskakis D J 2010 Matter-wave dark solitons: stochastic versus analytical results *Phys. Rev. Lett.* **104** 174101

[47] Busch T and Anglin J R 2000 Motion of dark solitons in trapped Bose-Einstein condensates *Phys. Rev. Lett.* **84** 2298–301

[48] Li W, Haque M and Komineas S 2008 Vortex dipole in a trapped two-dimensional Bose-Einstein condensate *Phys. Rev.* A **77** 053610

[49] Middelkamp S, Kevrekidis P G, Frantzeskakis D J, Carretero-González R and Schmelcher P 2010 Bifurcations, stability and dynamics of multiple matter-wave vortex states *Phys. Rev.* A **82** 013646

[50] Mithun T, Carretero-González R, Charalampidis E G, Hall D S and Kevrekidis P G 2022 Existence, stability, and dynamics of monopole and alice ring solutions in antiferromagnetic spinor condensates *Phys. Rev.* A **105** 053303

[51] Gaunt A L, Schmidutz T F, Gotlibovych I, Smith R P and Hadzibabic Z 2013 Bose-Einstein condensation of atoms in a uniform potential *Phys. Rev. Lett.* **110** 200406

[52] Tsitoura F, Anastassi Z A, Marzuola J L, Kevrekidis P G and Frantzeskakis D J 2016 Dark solitons near potential and nonlinearity steps *Phys. Rev.* A **94** 063612

[53] Aycock L M, Hurst H M, Efimkin D K, Genkina D, Lu H I, Galitski V M and Spielman I B 2017 Brownian motion of solitons in a Bose-Einstein condensate *Proc. Natl Acad. Sci.* **114** 2503–8